Research Article

Lixiang Fu, Jingling Ma*, Zhikang Zhang, Guangxin Wang*, Yuliang Liu, and Wuhui Li

Self-template synthesis of hollow flower-like NiCo₂O₄ nanoparticles as an efficient bifunctional catalyst for oxygen reduction and oxygen evolution in alkaline media

https://doi.org/10.1515/ntrev-2023-0103 received May 17, 2023; accepted July 12, 2023

Abstract: A method was proposed to synthesize hollow flower-like NiCo₂O₄ composed of porous nanosheets using a self-template approach. The unique structure is attributed to the synergistic effect of the Kirkendall effect and the Ostwald ripening mechanism. The sheet-like and porous structure endowed the material with a specific surface area of 137.1 m² g⁻¹ and a pore volume of 0.418 cm³ g⁻¹. The distinctive structure and high-density active sites imparted excellent catalytic performance in oxygen reduction (ORR) and oxygen evolution (OER) reactions. Electrochemical tests showed that the limit current density of ORR reached 5.58 mA cm⁻², comparable to that of the noble metal Pt/C (20 wt%). The overpotential of OER at a current density of 10 mA cm⁻² was only 380 mV, significantly lower than that of the noble metal RuO2. These results indicate that the synthesized hollow flower-like NiCo₂O₄ has the potential to replace noble metals in ORR and OER catalytic applications.

Lixiang Fu, Zhikang Zhang: Research Center for High Purity Materials, Henan University of Science and Technology, Luoyang, 471023, China **Yuliang Liu, Wuhui Li:** Research Center for High Purity Materials, Henan University of Science and Technology, Luoyang, 471023, China; Collaborative Innovation Center of Nonferrous Metals, Henan University of Science and Technology, Luoyang, 471023, Henan Province, China

Keywords: self-template, hollow flower-like, Kirkendall effect, Ostwald ripening, oxygen evolution, oxygen reduction

1 Introduction

In recent years, there has been a rapid advancement in energy technology with the development of industries. However, the extensive use of non-renewable resources causes environmental pollution on a global scale [1,2]. Therefore, the utilization of efficient and clean energy sources is a future development trend [3]. Renewable energy sources such as solar, wind, hydro, and tidal power are being extensively developed and utilized, which has led to a more widespread application of energy conversion devices. For instance, the currently popular lithium-ion batteries are widely used in various aspects of life [4,5]. However, a new emerging energy technology has recently gained significant attention and is considered highly promising to replace lithium-ion batteries in the future due to the high cost and explosion risk of lithium-ion battery. This energy conversion device is the rechargeable metal-air battery [6]. Compared with current lithium-based battery technologies, metal-air batteries have significant advantages, such as high energy density and a flat discharge voltage profile, which make them more widely applicable in various fields. This greatly increases their potential for large-scale commercialization [7,8]. However, the slow oxygen evolution (OER) and oxygen reduction (ORR) reactions during the charge and discharge processes severely restrict the development of metal-air batteries [9]. Therefore, catalysts are needed to accelerate ORR and OER. Most commercially available metal-air batteries currently rely on the use of noble metal catalysts, which are hindered by their scarcity, expensive cost, and other limitations, preventing the widespread commercialization of metal-air batteries. Additionally, similar issues are encountered in other energy conversion devices

^{*} Corresponding author: Jingling Ma, Research Center for High Purity Materials, Henan University of Science and Technology, Luoyang, 471023, China; Collaborative Innovation Center of Nonferrous Metals, Henan University of Science and Technology, Luoyang, 471023, Henan Province, China, e-mail: majingling2018@163.com

^{*} Corresponding author: Guangxin Wang, Research Center for High Purity Materials, Henan University of Science and Technology, Luoyang, 471023, China; Collaborative Innovation Center of Nonferrous Metals, Henan University of Science and Technology, Luoyang, 471023, Henan Province, China, e-mail: wanggx2016@126.com

such as electrolysis cells, emphasizing the urgent need for the development of efficient non-noble metal catalysts [10].

Transition-metal oxides (TMOs) possess characteristics such as high reserves, easy preparation, stability, and high activity, making them widely recognized as the most promising candidates to replace noble metal catalysts [11]. However, due to the excessive or insufficient binding with the intermediate oxygen, TMOs are only conducive to one of the two oxygen reactions [12]. Consequently, they have only a single catalytic function, which is not in line with our pursuit of a dual-functional catalyst. To address this issue, researchers have introduced secondary metal substituents by composition modification to optimize the electronic properties of active sites and have also used material nano-engineering to regulate the morphology, porosity, and specific surface area of the material to increase the exposure of active sites during catalysis [13]. NiCo₂O₄ is a spinel-structured binary metal oxide with rich multiple oxidation states formed by the substitution of one Co atom on Co₃O₄ with a Ni atom [14]. The doping of Ni effectively modulates the electronic structure of Co₃O₄, resulting in better electrochemical performance compared to single TMOs [7]. In addition, the highly redox-coupled Co²⁺/Co³⁺ and Ni²⁺/Ni³⁺ in NiCo₂O₄ catalyst are considered as the active sites for OER [15]. The synergistic effect of Ni and Co endows NiCo₂O₄ with great catalytic performance. For example, the nanowire structure NiCo₂O₄ was prepared by Prabu et al. [16] and evaluated for its ORR performance in a 0.1 M KOH electrolyte solution. The linear voltammetric scan curve of linear sweep voltammetry (LSV) at 1,600 rpm exhibited a diffusion-limited current density of 6 mA cm⁻² and a half-wave potential of 0.78 V_{vsRHE}. Under equivalent conditions, the catalytic activity of ORR has approached that of noble metals. Furthermore, in the OER test, a current density of 10 mA cm⁻² was achieved at a potential of only $1.62\,V_{vsRHE}$ which is also superior to that of noble metal catalysts. Devaguptapu et al. prepared nanoneedle [17], spherical, and sea urchin-like NiCo₂O₄ using the template-free, hard-template, and soft-template methods, respectively. In electrochemical testing, NiCo₂O₄ with different morphologies exhibited varying catalytic activities. Additionally, researchers have designed numerous intriguing morphological structures of NiCo₂O₄. For instance, Zhang et al. synthesized core-shell structured NiCo₂O₄ using a hard template method [18]. Wei, by pre-adjusting the pH value, grew NiCo₂O₄ nanosheet arrays on graphene through a co-precipitation approach [19]. Similarly, Sun utilized a hydrothermal method to grow NiCo2O4 nanosheets and nanoflowers on nickel foam [20]. Different morphologies confer distinct characteristics to the materials [21], modifying the material's shape is a common means of improving

the performance of the catalyst. Among the many morphologies, sheet-like structures tend to have a large specific surface area, which allows the catalysts to expose the active site to a large extent during catalysis. However, most of the currently available fabrication methods are complex and time-consuming, which leads to a waste of time. Moreover, the sheet-like structure, due to its two-dimensional nature, tends to experience severe aggregation during the electrocatalytic process. This phenomenon can lead to a decrease in electron transfer rate, affecting charge transfer efficiency and the contact between active sites and electrolyte, resulting in reduced catalytic activity [22].

Based on the above considerations, this study prepared a hollow flower-like structure of ${\rm NiCo_2O_4}$ nanomaterials assembled from porous nanosheets using a self-template method. This preparation method is not only concise and effective, but the unique flower-like structure produced by this method also addresses the issue of nanosheet aggregation. The best-performing sample (NiCo-300) exhibited ORR catalytic activity comparable to that of the noble metal Pt/C and OER catalytic activity and significantly exceeded that of the noble metal ${\rm RuO_2}$ in the electrochemical tests.

2 Experimental section

2.1 Synthesis of nickel-cobalt glycerate microspheres (NiCo-G)

In a typical method [23], mix $0.25 \, \text{mmol Co}(\text{NO}_3)_2 \cdot 6\text{H}_2\text{O}$, $0.125 \, \text{mmol Ni}(\text{NO}_3)_2 \cdot 6\text{H}_2\text{O}$, and $8 \, \text{mL}$ of glycerol in $40 \, \text{mL}$ of isopropanol by stirring vigorously to form a uniform pink solution. Transfer the resulting solution to a stainless steel autoclave and keep it at 180°C for $6 \, \text{h}$. After cooling to room temperature, the brown precipitate was subjected to centrifugal separation at a speed of $10,000 \, \text{rpm}$ using a centrifuge, then washed with an alcohol solution $3-5 \, \text{times}$. Finally, vacuum dry the obtained solid powder at 60°C for $8 \, \text{h}$, and name the resulting solid powder as NiCo-G.

2.2 NiCo-G is transformed into hollow flower-shaped nickel-cobalt hydroxide (NiCo-OH)

Mix 20 mg NiCo-G with 40 mL of deionized water and stir vigorously. Transfer the evenly mixed solution into a stainless steel autoclave and maintain a constant temperature

of 150°C for 180 min. After cooling to room temperature, wash and dry the precipitate with alcohol for 2-3 times, and vacuum dry it in a drying oven at 60°C for 8 h. Finally, the solid product is recorded as NiCo-OH.

2.3 Preparation of hollow flower-like NiCo₂O₄ materials from NiCo-OH

NiCo-OH was heated in an air atmosphere at 300°C for 2 h in a tube furnace, and the resulting black powder NiCo₂O₄ was labeled as NiCo-300. To analyze the effect of heat treatment temperature on the morphological characteristics of the retained matrix (NiCo-OH) of NiCo₂O₄, NiCo-OH was subjected to heat treatment at 250 and 350°C for 2 h, respectively. The resulting samples were labeled as NiCo-250 and NiCo-350, respectively. The experimental procedures were thoroughly documented to ensure reproducibility.

2.4 Characterization

Different stages of the products were traced and observed for their morphology using field emission scanning electron microscopy (JSM-7800F). Thermal gravimetric (TG) analysis was carried out using a TA-Q600 thermal analyzer with a heating rate of 10°C/min. X-ray diffraction (XRD, Bruker-AXS D8 Advance) and transmission electron microscopy (TEM, JEM-2100) were employed for phase and structural analysis of NiCo₂O₄. X-ray photoelectron spectroscopy (XPS) was used to analyze the atomic valence states and their relative contents. The pore size distribution and specific surface area of the pyrolysis products were analyzed using a Quantachrome Autosorb IQ3 automated surface area analyzer.

2.5 Electrochemical experiments

The ORR and OER performances were evaluated using a PINE rotating disk electrode system and an electrochemical workstation (CHI660E). A glassy carbon electrode was used as the working electrode, a platinum plate was used as the counter electrode, and an Ag/AgCl electrode was used as the reference electrode. The electrochemical techniques employed included cyclic voltammetry (CV), LSV, stability testing (i-t), and electrochemical impedance spectroscopy (EIS). The working electrode was coated with a loading of 0.27 mg cm^{-2} (NiCo₂O₄:C = 7:1), and the electrolyte solution used was 0.1 M KOH. The measured potential was converted to the reversible hydrogen electrode (RHE) scale using the Nernst equation:

$$E_{\text{RHE}} = E_{\text{vs}} \text{ Ag/AgCl} + 0.0592 \text{ pH} + 0.2046.$$

3 Results and discussion

The preparation of the hollow flower-like NiCo-300 includes three steps. In the first step, Ni(NO₃)₂·6H₂O and Co(NO₃)₂·6H₂O provide nickel and cobalt sources. Under the high temperature and high pressure conditions of a solvent-thermal process. NiCo-G solid microspheres are formed. The second step is to convert NiCo-G into NiCo-OH with a hollow flower-like structure assembled from nanosheets based on the easy hydrolysis of metal glycerides. This process is a simple hydrolysis reaction of metal alcohols. The Ni²⁺, Co²⁺, and OH⁻ generated from the hydrolysis reaction will form a mixed nickelcobalt hydroxide (Ni_xCo_{2x}(OH)_{6x}) on the surface of the sphere based on the close solubility product constant (K_{sp}) of Ni(OH)₂ and Co(OH)₂ [24]. The generation process of (Ni_xCo_{2x}(OH)_{6x}) can be described as follows [25]:

$$NiCo-G \rightarrow Ni^{2+} + Co^{2+} + OH^{-},$$
 (1)

$$Ni^{2+} + Co^{2+} + OH^{-} \rightarrow Ni_{x}Co_{2x}(OH)_{6x}$$
 (2)

The third step in the preparation of the hollow flowerlike of NiCo₂O₄ involves the heat treatment of NiCo-OH obtained from the previous step in an air atmosphere at 300°C. The reaction process can be described as follows [25]:

$$Ni_{x}Co_{2x}(OH)_{6x} + O_{2} \rightarrow NiCo_{2}O_{4} + H_{2}O.$$
 (3)

3.1 Transformation of NiCo-G solid spheres to hollow flower-like NiCo-OH

The solid microspheres NiCo-G were transformed into a hollow flower-like NiCo-OH, and this transformation process occurred in a 150°C hydrothermal environment. The XRD pattern (Figure S1) recorded the success of this transformation. Although the transformation is a simple hydrolysis reaction, the formation of the hollow flower-like structure is worth investigating. In order to accurately analyze the formation of the hollow flower-like NiCo-OH, the morphology and structure of the products of NiCo-G hydrolyzed for 0, 15, 60, and 180 min were observed by TEM and scanning electron microscopy (SEM). In addition, the TEM image of the product obtained after hydrolysis of NiCo-G under room temperature and pressure was also observed. These results are shown in Figure 1(a)-(e) (also

please refer to Figures S1-S5). Figure 1(a) shows the TEM image of NiCo-G obtained by the solvothermal method. The image reveals that NiCo-G (i.e., NiCo-G hydrolyzed for 0 min) is a solid sphere with a smooth surface, which is consistent with the observations from the SEM image (Figure S2) of NiCo-G. TEM images of the product obtained from the hydrolysis of NiCo-G for 15 min clearly show the growth of a large number of nanosheets on the surface of the spherical particles, while no significant changes are observed in the interior of the particles (Figure 1(b)). The SEM image (Figure S3) clearly shows the existence of nano flakes on the surface of the solid sphere. Additionally, two spheres were observed without nano flakes on their surfaces, but with varying sizes of protrusions on the sphere's surface, which can be considered as the process experienced before the formation of the nanosheets. After 60 min of hydrolysis of NiCo-G, TEM images of the product reveal the presence of a structure inside the sphere that resembles

a core-shell structure, with a noticeable gap between the core and the shell (Figure 1(c)). The SEM image (Figure S4) clearly shows an increase in the number of nanosheets compared to that of 15 min of hydrolysis, and confirms the existence of the inner core, consistent with the TEM image (Figure 1(c)). The TEM image of the product obtained after 180 min of hydrolysis of NiCo-G is shown in Figure 1(d). It is evident from the image that the inner core of the sample has completely disappeared, forming a hollow structure. The hollow structure inside the sample is also observed in its SEM image (Figure 1(e)). Observation of the TEM images of the products obtained after hydrolysis of NiCo-G for 15, 60, and 180 min showed the presence of distinct black rods, which were caused by the intersection of nanosheets. This phenomenon of nanosheet intersection can be observed in SEM images as well. The width and length of the black rods indirectly reflect the thickness and length of the nanosheets. The data obtained through measurements are shown in

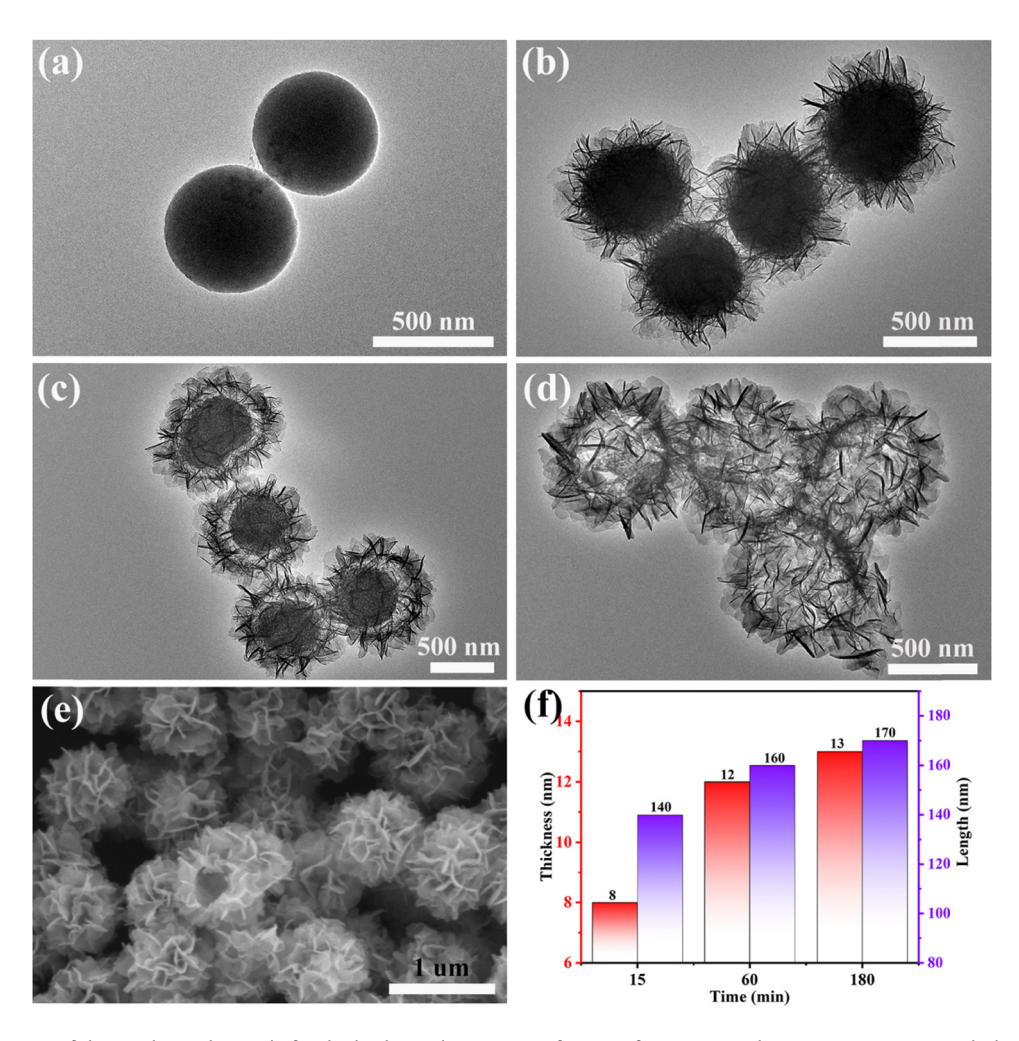


Figure 1: TEM image of the products obtained after hydrothermal treatment of NiCo-G for (a) 0 min, (b) 15 min, (c) 60 min, and (d) 180 min. (e) SEM image of the products obtained after hydrothermal treatment of NiCo-G for 180 min. (f) The thickness and length of nanosheets.

Figure 1(f). It can be observed that the formation of cavity structures is accompanied by the growth of nanosheets. This process (NiCo-G \rightarrow NiCo-OH) also occurs in the so-called self-template, where NiCo-G not only serves as a precursor but also templates itself to form this unique hollow flower-like structure. Furthermore, the samples exhibited a high degree of monodispersity, which may be attributed to the structural and state changes on the surface of the nanoparticles under the conditions of high temperature and high pressure during the solvothermal process [26]. This will facilitate the catalyst's full contact with the electrolyte during the catalytic process, exposing more active sites and enhancing catalytic activity.

Based on the above results, the possible mechanism for the formation of the hollow flower-like structure is shown in Figure 2. The formation of the hollow floral structure can be roughly divided into two stages. The first stage involves the formation of nanosheet-based structures. In the initial stage of the hydrolysis reaction, NiCo-G undergoes hydrolysis to form nickel-cobalt hydroxide nuclei. Under the influence of Ostwald ripening behavior [27,28], the small nuclei gradually gather on the surface of the sphere and grow into larger nanosheet-based structures. This phenomenon can be observed in the morphology presented by the sample at 15 min after the hydrolysis reaction. The second stage involves the formation of cavity structures. With the increase in hydrothermal time, a dense NiCo-OH shell is formed on the surface of the sphere. The presence of this shell controls the diffusion of Ni, Co, and water between each other [29]. When the outward

diffusion rate of nickel and cobalt is much faster than the inward diffusion rate of water, net outward diffusion of nickel and cobalt creates some vacancies at the interface of NiCo-G and NiCo-OH. As NiCo-G is consumed, these small vacancies combine to form cavities (as observed in samples at 60 and 180 min hydrolysis time) [7,30]. This formation of voids due to the imbalance in diffusion rates is a manifestation of the Kirkendall effect [31]. The formation of a nickel-cobalt hydroxide shell takes a certain amount of time. Therefore, the Kendall effect cannot occur during the initial stages. This is also the reason why no vacancy formation was observed in the product obtained after 15 min of hydrolysis of NiCo-G. Furthermore, based on the morphology exhibited by NiCo-G during hydrolysis at room temperature and pressure (Figure S5), it can be inferred that the occurrence of the Kirkendall effect (i.e., the formation of cavity structures), requires high temperature and pressure conditions. Under such conditions, it may be advantageous for the formation of a dense nickel-cobalt hydroxide shell or to accelerate the outward diffusion of nickel and cobalt. Based on the previous discussion, it can be concluded that the formation of the hollow flower-like structure is closely related to the hydrothermal reaction time. During the initial stage of the hydrothermal reaction, the Ostwald ripening mechanism dominates the growth of the nanoplates. However, with the prolonged reaction time, the Kirkendall effect participates, leading to the formation of the hollow structure. The synergy of these two mechanisms provides the driving force for the formation of the hollow flower-like structure.

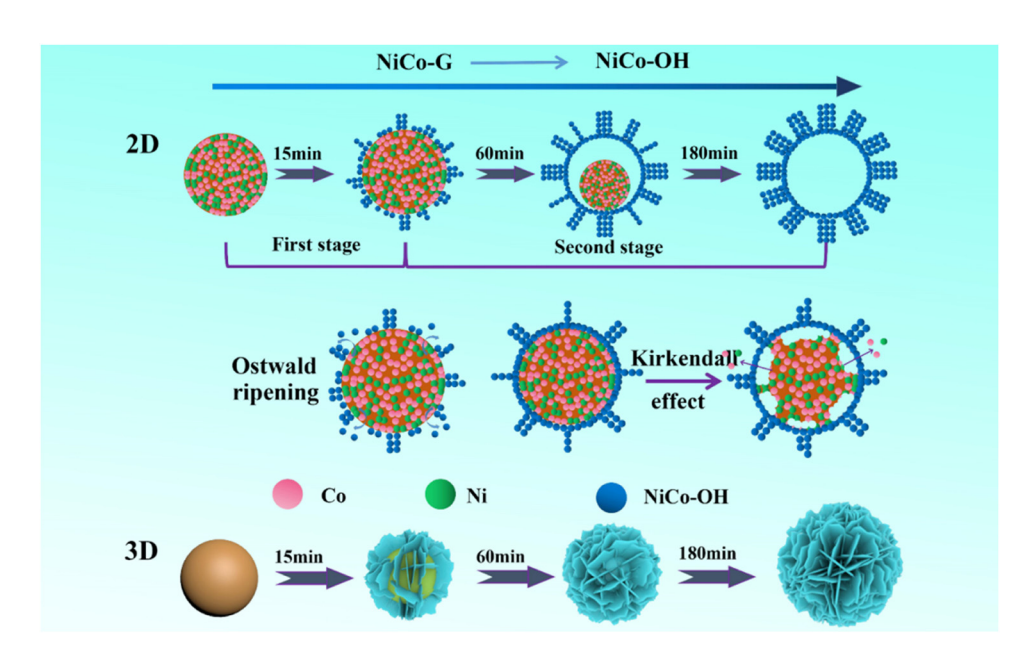


Figure 2: Schematic diagram of the transformation of NiCo-G to NiCo-OH.

6 — Lixiang Fu et al. DE GRUYTER

3.2 Formation of hollow flower-like NiCo₂O₄ (NiCo-300)

The formation process of NiCo₂O₄ was studied using TGA and differential thermal gravimetry (DTG) as shown in Figure 3(a). The TG curve represents the temperature range of sample quality loss, while the DTG curve shows the maximum mass loss rate of the sample [32]. Based on the TG/DTG curves, the thermal decomposition of NiCo-OH can be divided into two stages. The first stage is considered to be between 15 and 140°C, during which the DTG curve exhibits a prominent peak. This can be attributed to the rapid loss of mass caused by the escape of physically adsorbed water. In this stage, the mass loss is 10.8%. The second stage occurs between 140 and 400°C, where the DTG curve exhibits the highest peak. This peak corresponds to the rapid mass loss due to the conversion of NiCo-OH to NiCo₂O₄. In this stage, the sample experiences a mass loss of 21.6%. Beyond 400°C, the sample continues to lose mass without showing significant thermal stability. There are two possible reasons for this phenomenon. First, residual organic compounds in the sample undergo oxidation and decomposition with increasing thermal decomposition temperatures, resulting in sustained mass loss. Second, the material has slightly inferior thermal stability, indicating that the selection of the thermal treatment temperature is crucial. Figure 3(b) shows the XRD patterns of the products after heat treatment at different temperatures. It can be seen that NiCo-300 and NiCo-350 have very distinct diffraction peaks, and NiCo-350 has sharper and more symmetrical diffraction peaks. This indicates that the crystallinity of NiCo-350 is higher. The diffraction peaks at 31.15°, 36.70°, 44.63°, 59.11°, and 64.96° in both samples correspond to the (220), (311), (400), (511), and (440) crystal planes of NiCo₂O₄, respectively, which match the standard card of NiCo₂O₄

(JCPDS 20-0781) [33]. No impurity peaks are observed, indicating that NiCo-G is completely converted to $\rm NiCo_2O_4$ crystals under both temperatures. However, only three diffraction peaks are observed for NiCo-250, which cannot well prove the complete transformation of NiCo-G to NiCo₂O₄. This may affect the formation of active sites and thus affect the catalytic performance of the material. In addition, the grain sizes of NiCo-250, NiCo-300, and NiCo-350 were calculated using the Scherrer formula, resulting in sizes of 8.5, 10.2, and 12.5 nm, respectively. It can be observed that the grain size gradually increases with the increase in annealing temperature.

$$D = K\lambda/(B\cos\theta). \tag{4}$$

The products obtained from different temperature treatments were observed by SEM and TEM, as shown in Figure 4(a)–(f), (also see Figures S6–S10). Figure 4(a) shows the TEM image of NiCo-300, which reveals that the sample well inherits the hollow flower-like structure of the precursor material. The size of the porous nanosheets at this point mainly ranged around 140 nm in length and 10 nm in thickness, which decreased compared to NiCo-OH (around 170 nm in length and 13 nm in thickness). This is due to material shrinkage during the heat treatment process. However, some broken porous nanosheets were also observed, which cannot be clearly displayed on the hollow nanoflowers (Figure S6). High-resolution transmission electron microscopy (HRTEM) images (Figure 4(b)) reveal that the porous nanosheets are composed of small crystalline particles, and the escape of CO₂ and H₂O during the heat treatment of NiCO-G leads to the presence of abundant pores in the porous nanosheets [24]. Figure 4(c) shows the mesopores, which are mainly distributed in the range of 2-8 nm, and each size of mesopores has a certain number of distribution. The pore structure not only provides a larger surface area for the catalyst,

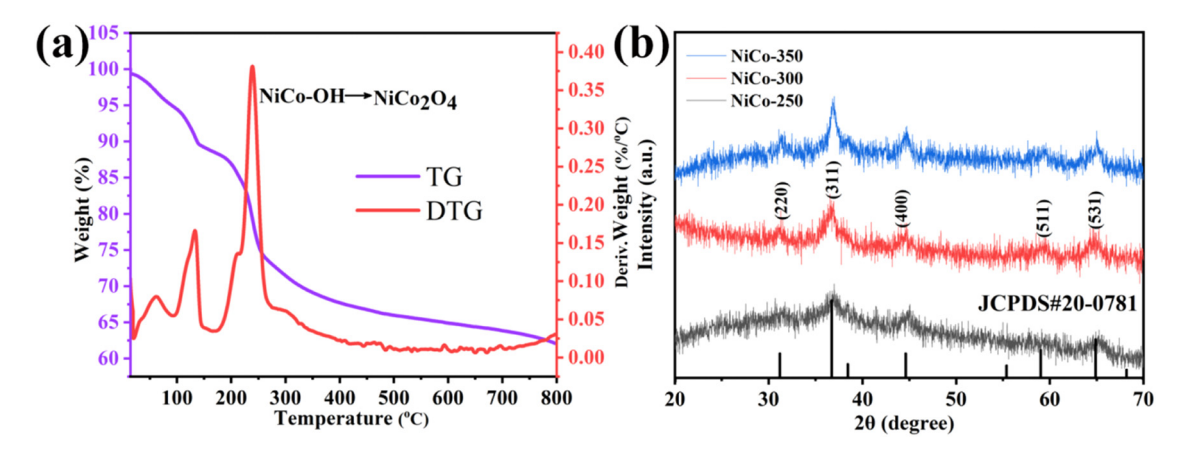


Figure 3: (a) TG curve of NiCo-OH measured in air and DTG curve obtained by differentiating the TG curve and (b) XRD patterns.

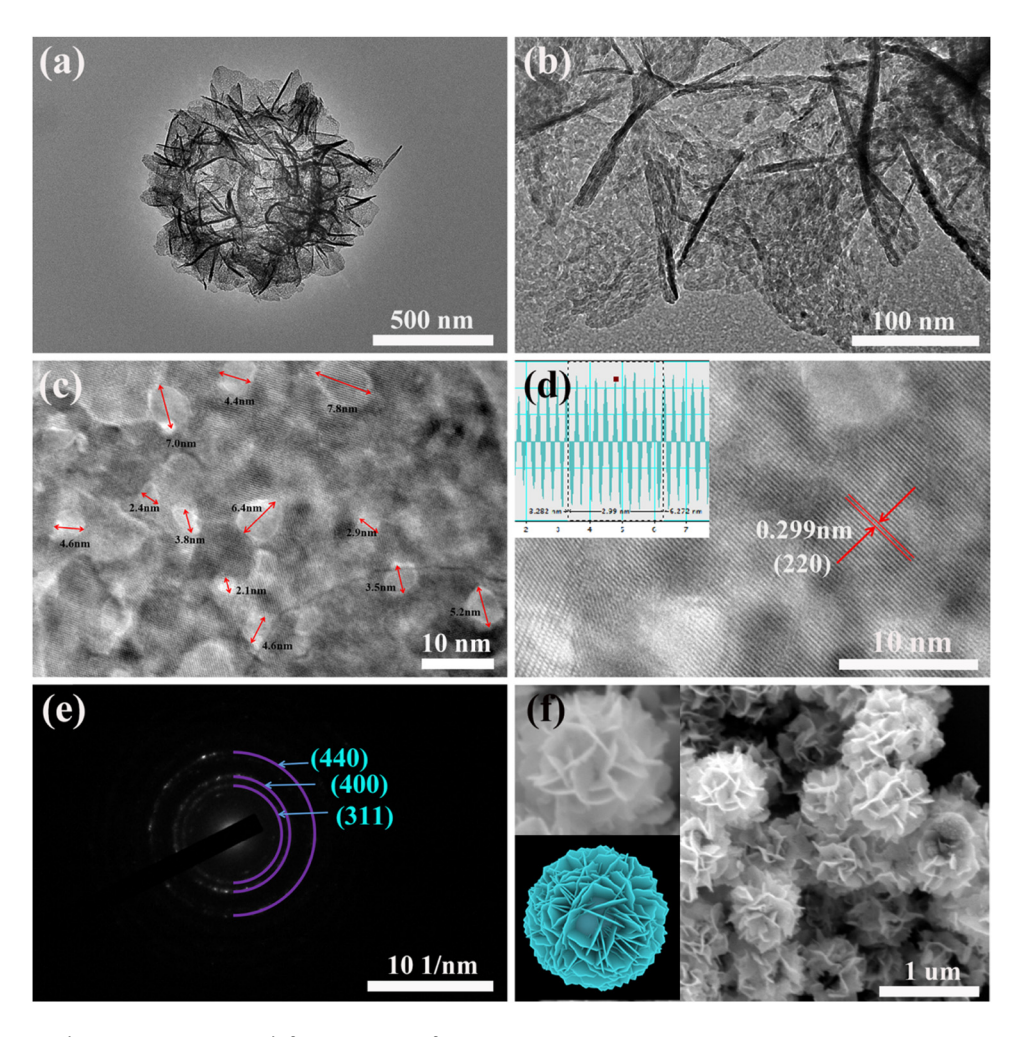


Figure 4: (a-c) TEM, (d) HRTEM, (e) SAED, and (f) SEM images of NiCo-300.

but also provides a shorter path for ion transfer, which improves the efficiency of the catalyst. HRTEM image clearly shows lattice fringes with a spacing of 0.299 nm, which is close to the spacing between the two (220) crystal planes of NiCo₂O₄ (Figure 4(d)). This also indicates the great crystallinity of the sample. Selected area electron diffraction (SAED) pattern clearly shows the polycrystalline nature of the sample, with diffraction rings matching well with the standard spinel NiCo₂O₄ (Figure 4(e)). The SEM image of NiCo-300 (Figure 4(f)) and the SEM image of NiCo-OH (Figure 1(e)) exhibit great similarity, which better illustrates that NiCo-300 well preserved the parent morphology of NiCo-OH. In addition, the TEM image of NiCo-250 (Figure S7(a)) shows that it also inherits the morphology of the parent material well. Figure S7(b) shows that the porous nanosheets of NiCo-250 have a higher mesoporous density than NiCo-300, with pore sizes concentrated at 3.4 nm, and fewer but relatively larger mesopores (the larger mesopores referred to in the text are those with a diameter greater than 3.4 nm). The SEM image of NiCo-

250 also demonstrates the preservation of the parent morphology (Figure S8). The TEM (Figure S9) and SEM (Figure S10) images of NiCo-350 indicate that the structure has collapsed and the porous nanosheets have disintegrated and broken, failing to inherit the morphology of the parent material. These results indicated that the preservation of the matrix morphology in NiCo2O4 was influenced by the heat treatment temperature, with higher temperature being detrimental to parent morphology preservation. One possible reason is that as the heat treatment temperature increases, larger pores are created when CO₂ and H₂O escape during the heat treatment process, and excessively large mesopores are detrimental to structural stability.

The porosity and pore size of NiCo-T were characterized using the nitrogen adsorption/desorption method. NiCo-300 exhibits hysteresis loops in the range of 0.5–1.0. Meanwhile, all the isotherm profiles belong to Type IV, indicating the presence of a porous structure [34]. This observation is further confirmed by the TEM images. 8 — Lixiang Fu et al. DE GRUYTER

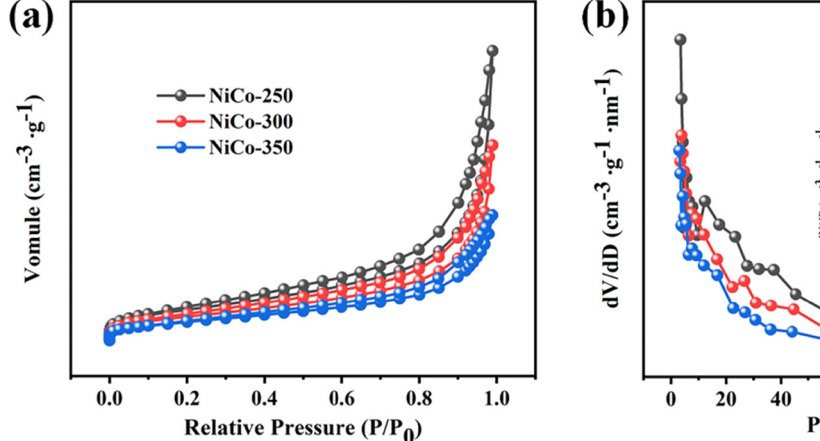
Table 1: Specific surface area and pore volume of NiCo-300

Catalysts	Specific surface area (m² g ⁻¹)	Pore volume (cm³ g ⁻¹)
NiCo-250	173.8	0.627 0.418
NiCo-300 NiCo-350	137.1 108.1	0.418

According to the desorption isotherms and Brunauer-Emmett-Teller method, the specific surface areas of NiCo-250, NiCo-300, and NiCo-350 were calculated to be 173.8, 137.1, and 108.1 m² g⁻¹, respectively (Table 1). These results are superior to those previously reported for NiCo₂O₄ with different morphologies (Table S1). The pores on the porous nanosheets are closer to cylindrical in shape, so the pore size distribution plot was obtained using the Barrett-Joyner-Halenda (BJH) method (Figure 5(b)). Using the BJH method, the pore volumes of NiCo-250, NiCo-300, and NiCo-350 were calculated to be 0.627, 0.418, and 0.270 cm³ g⁻¹, respectively. From the Figure, it can be seen that NiCo-300 has more number of larger mesopores compared to NiCo-250 (consistent with the results shown by TEM). However, the pore volume of NiCo-300 is lower than that of NiCo-250. This can be attributed to two possible reasons: first, NiCo-300 has a significantly lower pore density than NiCo-250. Second, a small portion of the porous nanosheets in NiCo-300 may have been broken. resulting in loss of pore structure. Both of these factors are clearly observed in the TEM images of the two materials. Pore volume greatly affects the specific surface area of the material, which is why NiCo-300 and NiCo-250 have different specific surface areas despite retaining their original

morphologies. The decrease in the specific surface area of NiCo-350 is attributed to the collapse of its structure and the fragmentation of its porous nanosheets.

The oxidation state and chemical composition of NiCo-300 were analyzed by XPS, as shown in Figure 6(a). The test spectrum showed the presence of Co, Ni, O, and C in the sample, without the appearance of any other impurities. In order to further analyze the valence state of the elements, high-resolution XPS analysis was carried out as shown. Figure 6(b) shows the high-resolution O1S spectrum, with three different binding energy peaks corresponding to O1 (529.5 eV), O2 (531 eV), and O3 (532.5 eV), respectively. The presence of the O1 peak can be attributed to the metaloxygen bond (M-O-M, M = Ni, Co) [35,36]. The O2 peak corresponds to the abundant low-oxygen coordinated defect sites, which promote the adsorption of water and OH [37]. This enables the catalyst to have a more thorough contact with the electrolyte, promoting the adsorption of oxygen. The O3 peak can be assigned to the oxygen adsorbed by water molecules on the surface of the material [38]. Figure 6(c) shows the high-resolution Ni 2p spectrum, which has been fitted into two orbital spin states (Ni $2p^{1/2}$ and Ni $2p^{3/2}$) using Gaussian fitting. It displays two oxidation states (Ni²⁺ and Ni³⁺) of Ni, with energy peak values of 854.1 and 871.6 eV assigned to Ni²⁺, and energy peak values of 855.8 and 873.4 eV assigned to Ni³⁺. Two satellite peaks (Sat.) are located at 861.4 and 879.6 eV. Figure 6d shows the high-resolution Co 2p spectrum, which has also been fitted into two orbital spin states (Co 2p^{1/2} and Co 2p^{3/2}) using Gaussian fitting. It represents two oxidation states (Co²⁺ and Co³⁺) of Co, with energy peak values of 781.7 and 796.4 eV assigned to Co²⁺, and energy peak values of 779.7 and 794.9 eV assigned



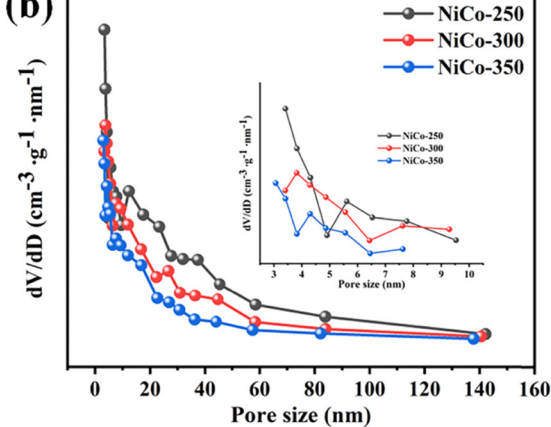


Figure 5: (a) N₂ adsorption-desorption isotherms and (b) pore size distribution curves of NiCo-T.

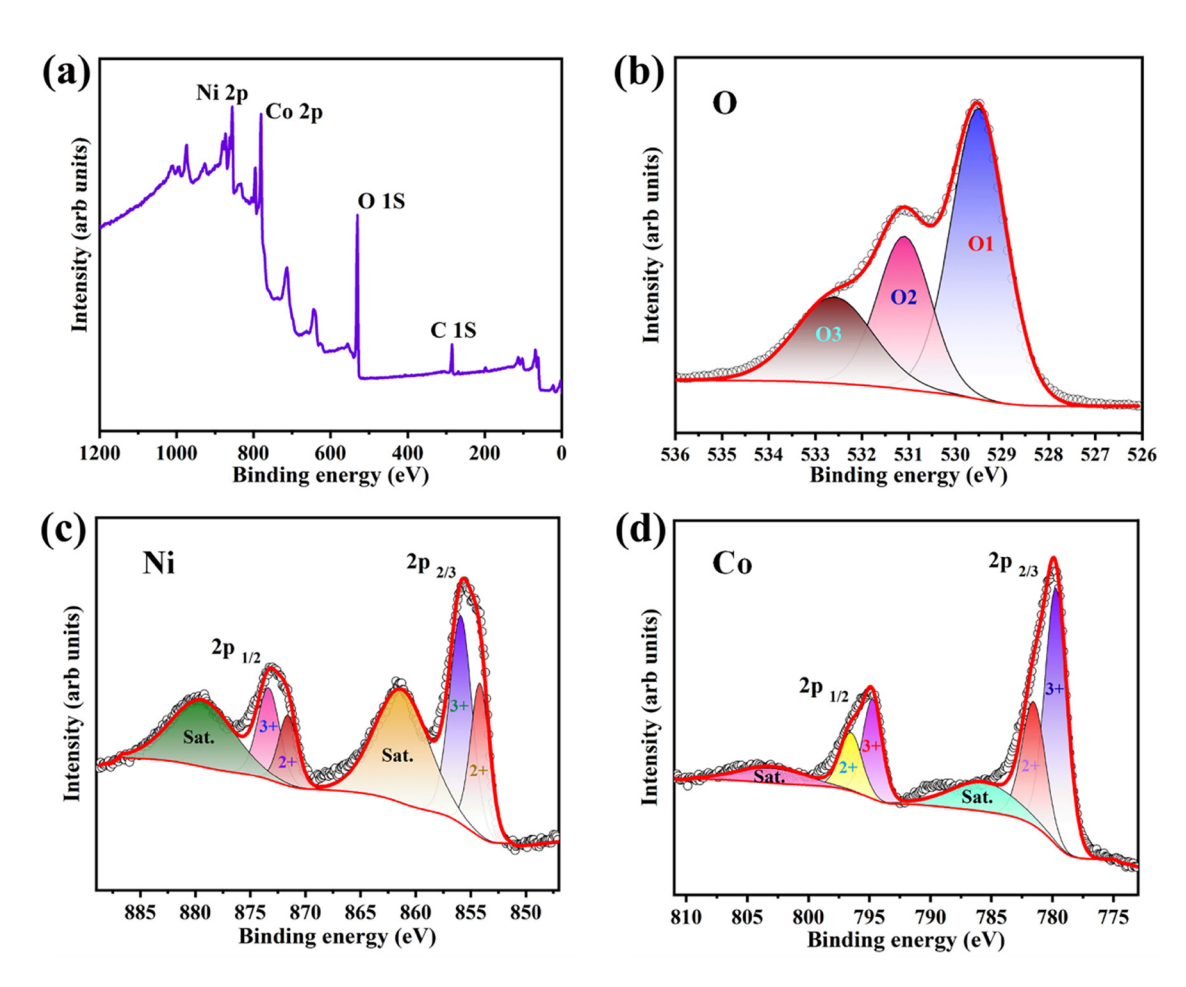


Figure 6: (a) XPS survey spectra of NiCo-300. High-resolution XPS spectra of (b) O 1 s, (c) Ni 2p, and (d) Co 2p.

to Co³⁺ [39]. Energy peak values of 786.2 and 802.9 eV are assigned to two satellite peaks. The XPS spectra indicate that the NiCo-300 material contains Ni³⁺, Ni²⁺, Co³⁺, and Co²⁺, which is consistent with previous data obtained by researchers [40,41]. The quantified contents of Ni²⁺, Ni³⁺, Co²⁺, and Co³⁺ determined by XPS spectroscopy (Table 2) indicate that the concentrations of Ni³⁺ and Co³⁺ are higher than those of Ni²⁺ and Co²⁺, suggesting the presence of oxygen vacancies in NiCo-300. The existence of oxygen vacancies has been proven to greatly enhance the ORR/OER catalytic activity of catalysts [42]. Additionally, the presence of oxygen vacancies enhances the efficiency of charge transport, which promotes the electrical conductivity of semiconductor materials [43]. The oxygen vacancies endow the material with

Table 2: Contents of Ni²⁺, Ni³⁺, Co²⁺, and Co³⁺

DE GRUYTER

	2 ⁺	3 ⁺
Со	28.4%	71.6%
Ni	35.5%	64.5%

great electrochemical properties, which will be further analyzed and validated through electrochemical tests.

3.3 Electrocatalytic activity of hollow flower-like NiCo₂O₄

In order to analyze the ORR catalytic performance of the hollow flower-like NiCo2O4, LSV was conducted in an oxygensaturated 0.1 M KOH electrolyte solution. In order to compare the differences in catalytic performance between materials and noble metals, identical tests were performed on Pt/C under the same conditions. The results are shown in Figure 7(a), which demonstrates that the ORR catalytic performance of the material varies under different temperature treatments. Figure 7(b) displays the half-wave potential and diffusion-limited current density of ORR for different samples according to Figure 7(a). NiCo-300 demonstrates the best performance with a half-wave potential ($E_{1/2}$) of 0.72 V_{vsRHE} and a diffusion-limited current density of 5.58 mA cm⁻², which is comparable to that of the noble metal Pt/C and even superior

in terms of diffusion-limited current density. In contrast, NiCo-250 and NiCo-350 have half-wave potentials ($E_{1/2}$) of only 0.7 and 0.65 V_{vsRHE}, and diffusion-limited current densities of only 5.16 and 4.92 mA cm⁻², respectively. The Tafel slope reflects the catalytic kinetics of the catalyst. The flatter the Tafel curve, the smaller the overpotential required for the catalytic reaction, which represents the fast kinetic of the ORR and indicates that the catalyst has superior performance in catalysis [44]. The great ORR performance of NiCo-300 is

reflected in the Tafel curve (NiCo-250: 91.1 mV dec⁻¹, NiCo-300: 88.5 mV dec⁻¹, NiCo-350: 101.9 mV dec⁻¹, Pt/C: 95.5 mV dec⁻¹) (Figure 7(c)). The fast ORR catalytic kinetics of NiCo-300 can be attributed to its good crystallinity and high specific surface area, which provide a large number of active sites, as well as the rapid charge transfer ability facilitated by oxygen vacancies. Figure 7(d) shows the LSV curve of NiCo-300 at 400–2,025 rpm. The results indicate that the limit diffusion current increases with the increase in the rotation

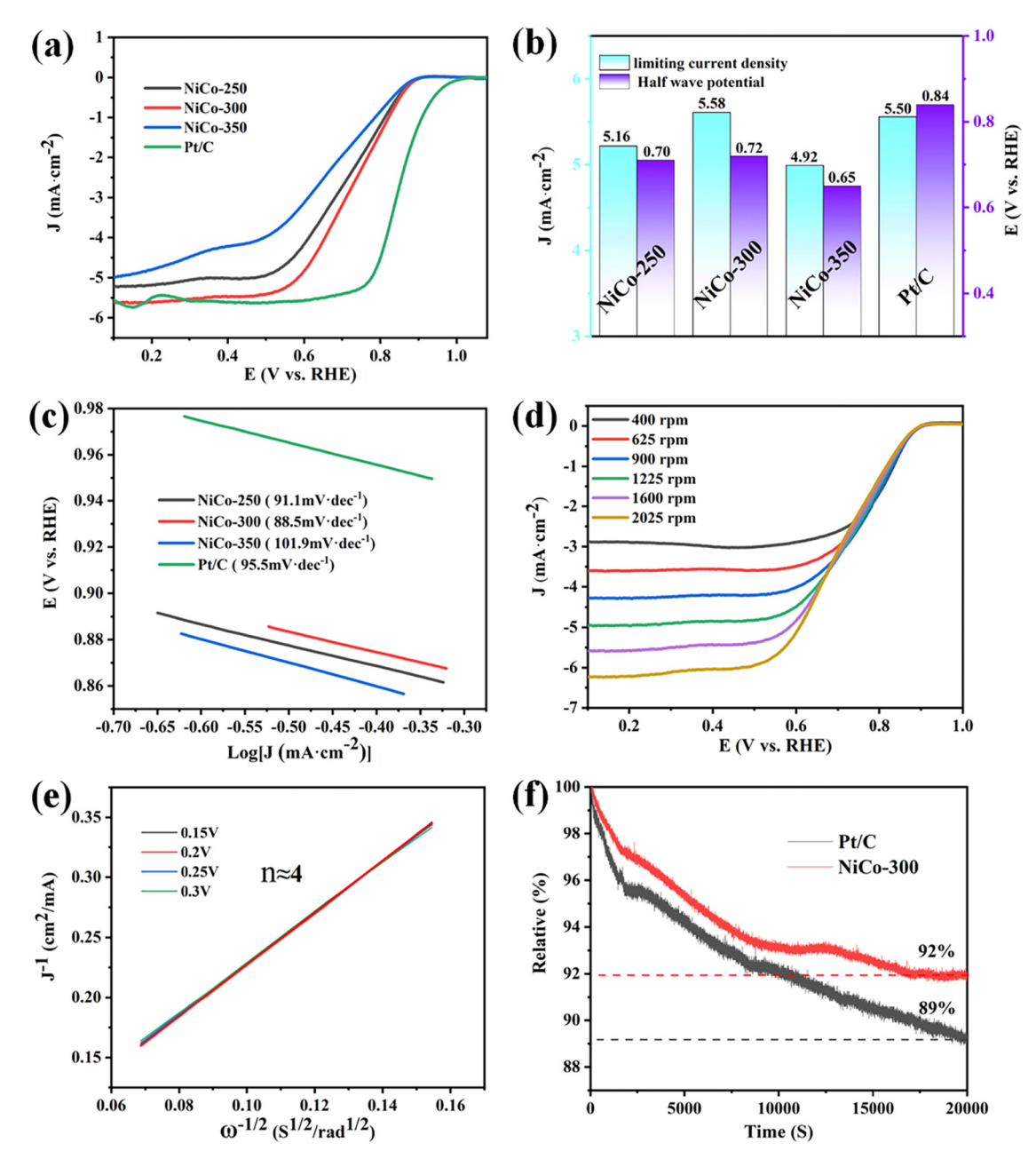


Figure 7: (a) ORR LSV curves of various catalysts, (b) diffusion-limited current density and half-wave potential of various catalysts, (c) ORR Tafel plots of various catalysts, (d) LSV curves of NiCo-300 at different rotation rates, (e) K–L curve of NiCo-300 at different potentials, and (f) *i–t* curves toward NiCo-300 and Pt/C.

speed, which suggests that the electrode surface has a fast oxygen flow and mass transfer capability at high speeds. The Koutecky–Levich (K–L) curve of NiCo-300 obtained from Figure 7(d) indicates a four-electron catalytic process, which demonstrates the great catalytic performance of NiCo-300 (Figure 7(e)). In order to investigate the stability of NiCo-300 during the ORR process, *i–t* test was carried out at a voltage of 0.6 V. The experiment was conducted in a

0.1 M KOH electrolyte solution with a rotation speed of 1,600 rpm, and Pt/C was also tested under the same conditions (Figure 7(f).). After 20,000 s test, the current of NiCo-300 decreased by only 8%, while the noble metal Pt/C lost 11%. This indicates that the catalytic stability of NiCo-300 is superior to that of the noble metal Pt/C. Although NiCo-300 is a hollow structure assembled from porous nanosheets, its catalytic stability is commendable. This is partly due to the

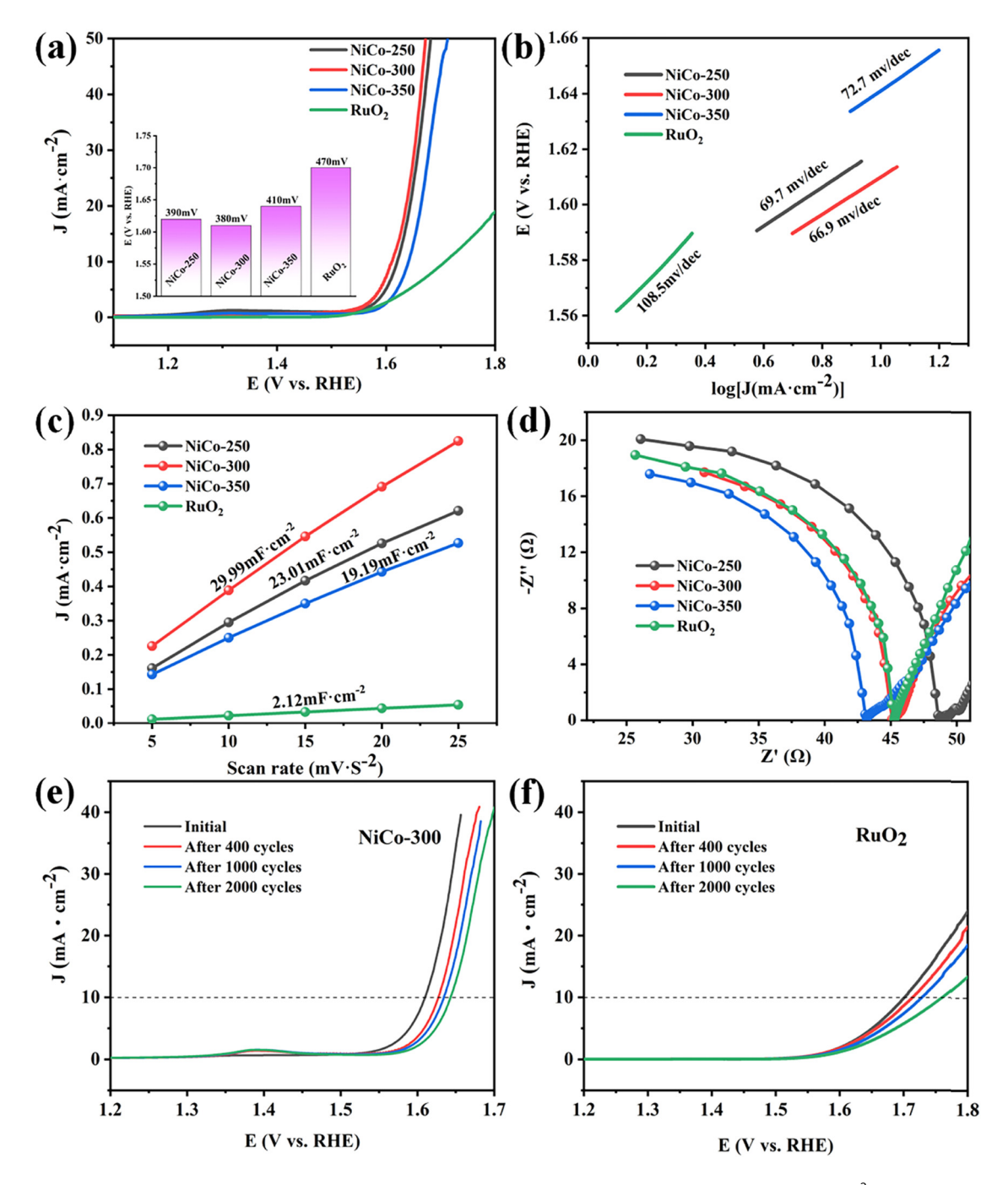


Figure 8: (a) OER LSV curves of various catalysts (insert: overpotential of various catalysts at a current density of 10 mA cm⁻²), (b) OER Tafel of various catalysts, (c) C_{dl} curves and (d) EIS curves. OER LSV curves after different numbers of CV cycles for (e) NiCo-300 and (f) RuO₂.

high stability of TMOs in alkaline solutions. The superior ORR catalytic performance of NiCo-300 is attributed to its high specific surface area (137.1 $\rm m^2\,g^{-1}$) and the high-density active sites provided by its spinel-structured NiCo₂O₄, which endows the catalytic reaction with great kinetic properties. Furthermore, the presence of oxygen vacancies changes the electrical conductivity of the material, accelerates the charge transfer during the catalytic process, and enhances the catalytic efficiency.

NiCo-300 performs well not only in ORR catalysis but also demonstrates significant activity in OER catalysis. This tested the electrocatalytic activity of the catalyst for OER in a 0.1 M KOH electrolyte solution. To compare with noble metals, the same tests were conducted on RuO2 under the same conditions, and the results are shown in Figure 8. The overpotential at 10 mA cm⁻² current density in OER LSV curves is widely recognized as an important parameter to measure the performance of OER catalysts [45]. A smaller overpotential represents a better OER performance of the catalyst. It can be seen that NiCo-300 has the minimum overpotential ($E_{j=10}$: 380 mV) at 10 mA cm⁻² current density compared to NiCo-250 (390 mV), NiCo-350 ($E_{i=10}$: 410 mV), and RuO_2 ($E_{j=10}$: 470 mV) in Figure 8(a). This indicates that NiCO-300 possesses the best OER catalytic activity and significantly outperforms the noble metal RuO₂. The flat Tafel slope curve of NiCo-300 also indicates the superior OER catalytic kinetics of NiCo-300 (Figure 8(b)). The double-layer capacitance ($C_{\rm dl}$) of the non-faradaic region was measured using CV. Cdl is positively correlated with the electrochemical active surface area (ECSA) [46]. As shown in Figure 8(c), NiCo-300 has the largest ECSA (29.99 mF cm⁻²). The EIS of the catalyst at open circuit potential in 0.1 M KOH electrolyte solution is shown in Figure 8(d). The radius in the high frequency region of the impedance spectrum is proportional to the impedance. It can be observed that the conductivity is improved with the increase in the annealing temperature. This may be due to the increased crystallinity of the material (Figure 3(b)). Figure 8(e) and (f) displays the LSV curves of NiCo-300 and RuO₂ after undergoing different numbers of CV cycles. It can be observed that even after 2,000 cycles, NiCo-300 exhibits a lower overpotential at 10 mA cm⁻² compared to RuO₂. While NiCo-300 exhibits slightly lower initial stability, its long-term stability is still superior to that of RuO₂. Based on the above, the OER catalytic performance of NiCo-300 is superior to that of RuO₂, suggesting its potential as a replacement.

NiCo-250 has a similar morphology to NiCo-300, and possesses a high specific surface area. However, NiCo-250 does not exhibit the best catalytic performance, possibly due to two reasons. First, the low annealing temperature of NiCo-250 may not result in a complete transformation to

NiCo₂O₄, which is evidenced by the XRD patterns (Figure 3(b)). This may have an impact on the formation of active sites. Second, NiCo-300 generally has larger mesopore size than NiCo-250, which can be observed from their respective TEM images and pore size distribution figures. Small mesoporous catalysts may reduce their catalytic activity by limiting the access of reactants to the catalytic sites or by reducing the number of active sites per unit area [47]. In contrast, larger pores are beneficial for the mass transfer of active species and the exposure of active sites during electrocatalysis [48]. The effect of pore size on the performance of catalysts has been confirmed by other researchers [49–51]. Based on these two considerations, the difference in ORR/OER catalytic performance between NiCo-250 and NiCo-300 is acceptable. Although NiCo-350 can be effectively converted to NiCo2O4, it does not exhibit superior ORR/OER catalytic activity due to its collapsed structure and low specific surface area.

The NiCo-300 catalyst exhibits the best ORR/OER catalytic performance, which is a comprehensive reflection of multiple factors. These factors can be considered as follows: (i) the hollow flower-like structure endows NiCo-300 with high specific surface area, exposing more active sites during the catalytic process; (ii) NiCo-G is well converted to the spinel structure of NiCo₂O₄, giving NiCo-300 high density of active sites; (iii) the suitable size mesopores formed by heat treatment provide ample space for mass transfer of the catalyst during the catalytic process.

4 Conclusion

In summary, a hollow flower-like structure of NiCo₂O₄ was successfully synthesized using a hydrothermal method, and the possible mechanisms responsible for the formation of this unique structure were discussed. This hollow flower-like NiCo2O4, synthesized by a self-template strategy, is assembled from porous nanosheets with a thickness of about 10 nm and a length of about 140 nm. In the subsequent ORR/OER catalytic activity tests, NiCo-300 exhibited the best performance. The results suggest that the hollow flower-like NiCo₂O₄ has the potential to replace noble metals such as Pt/C and RuO₂ in ORR and OER catalytic applications. The approach described in this study provides a promising strategy for developing efficient bifunctional catalysts for energy conversion devices such as metal-air batteries. Moreover, this synthesis strategy can provide reference for synthesizing hollow structures of other multicomponent TMOs, enabling the realization of specific functions.

Funding information: The authors acknowledge the financial support from the National Natural Science Foundation of China (Grant No. U1804146).

Author contributions: All authors have accepted responsibility for the entire content of this manuscript and approved its submission.

Conflict of interest: The authors state no conflict of interest.

References

- Makarieva AM, Gorshkov VG, Li B-L. Energy budget of the biosphere and civilization: Rethinking environmental security of global renewable and non-renewable resources. Ecol Complex. 2008;5(4):281-8.
- [2] Jia X, Ma J, Zhang C, Zhang Z, Fu L, Wang G. Gel polymer electrolyte with alkaline aquatic colloidal graphene for flexible and rechargeable zinc air batteries. Electrochim Acta. 2023;448:142195.
- Wang J, Zhang H, Hunt MRC, Charles A, Tang J, Bretcanu O, et al. Synthesis and characterisation of reduced graphene oxide/bismuth composite for electrodes in electrochemical energy storage devices. ChemSusChem. 2017;10(2):363-71.
- Stan A-I, Swierczynski M, Stroe D-I, Teodorescu R, Andreasen SJ. Lithium ion battery chemistries from renewable energy storage to automotive and back-up power applications - An overview. IEEE.
- Duan J, Tang X, Dai H, Yang Y, Wu W, Wei X, et al. Building safe lithium-ion batteries for electric vehicles: A review. Electrochem Energy Rev. 2020;3:1-42.
- Mondal A, Das HT, Mondal S, Sonkusare VN, Chaudhary RG. Emerging nanomaterials in energy storage. Mater Res Found. 2023:141:294-326.
- Zuo X, Chang K, Zhao J, Xie Z, Tang H, Li B, et al. Bubble-templateassisted synthesis of hollow fullerene-like MoS2 nanocages as a lithium ion battery anode material. J Mater Chem A. 2016;4(1):51-8.
- Wang Z-L, Xu D, Xu J-J, Zhang X-B. Oxygen electrocatalysts in metal-air batteries: From aqueous to nonaqueous electrolytes. Chem Soc Rev. 2014;43(22):7746-86.
- Cheng F, Chen J. Metal-air batteries: From oxygen reduction electrochemistry to cathode catalysts. Chem Soc Rev. 2012;41(6):2172-92.
- [10] Li Y, Dai H. Recent advances in zinc-air batteries. Chem Soc Rev. 2014;43(15):5257-75.
- [11] Guo Y, Chen Y-N, Cui H, Zhou Z. Bifunctional electrocatalysts for rechargeable Zn-air batteries. Chin J Catal. 2019;40(9):1298-310.
- [12] Seo MH, Park HW, Lee DU, Park MG, Chen Z. Design of highly active perovskite oxides for oxygen evolution reaction by combining experimental and ab initio studies. ACS Catal. 2015;5(7):4337-44.
- [13] Lee DU, Park MG, Cano ZP, Ahn W, Chen Z. Hierarchical core-shell nickel cobaltite chestnut-like structures as bifunctional electrocatalyst for rechargeable metal-air batteries. ChemSusChem. 2018;11(2):406-14.
- [14] Veeramani V, Madhu R, Chen S-M, Sivakumar M, Hung C-T, Miyamoto N, et al. NiCo₂O₄-decorated porous carbon nanosheets

- for high-performance supercapacitors. Electrochim Acta. 2017:247:288-95.
- [15] Zhang Y, Ma M, Yang J, Su H, Huang W, Dong X. Selective synthesis of hierarchical mesoporous spinel NiCo₂O₄ for high-performance supercapacitors. Nanoscale. 2014;6(8):4303-8.
- Prabu M, Ketpang K, Shanmugam S. Hierarchical nanostructured NiCo₂O₄ as an efficient bifunctional non-precious metal catalyst for rechargeable zinc-air batteries. Nanoscale. 2014;6(6):3173-81.
- Devaguptapu SV, Hwang S, Karakalos S, Zhao S, Gupta S, Su D, et al. Morphology control of carbon-free spinel NiCo2O4 catalysts for enhanced bifunctional oxygen reduction and evolution in alkaline media. ACS Appl Mater Interfaces. 2017;9(51):44567-78.
- Zhang Y, Xiao X, Zhang W, Liu Y, Zhong J, Chen M, et al. Facile formation of NiCo₂O₄ yolk-shell spheres for highly reversible sodium storage. J Alloy Compd. 2019;800:125-33.
- [19] Wei Z. Honeycombed-like nanosheet array composite NiCo₂O₄/rGO for efficient methanol electrooxidation and supercapacitors. Electrochim Acta. 2020;362:137145.
- [20] Sun B. Three-dimensional NiCo₂O₄ nanosheets and nanoflowers electrodeposited with palladium nanoparticles on nickel foam for the hydrogen evolution reaction. J Phys Chem Solids. 2021;158:110255.
- Lu J. Morphology control of nickel nanoparticles prepared in situ within silica aerogels produced by novel ambient pressure drying. Sci Rep. 2020;10(1):11743.
- Zhao L, Zhang G, Wang B, Li G. Hollow capsule NiCo₂NS prepared by self-sacrificing template method for high-efficiency bifunctional catalyst and its application in zn-air battery. Chem - Eur J. 2022;28(19):e202200036.
- [23] Shen L, Yu L, Yu X-Y, Zhang X, Lou XWD. Self-templated formation of uniform NiCo₂O₄ hollow spheres with complex interior structures for lithium-ion batteries and supercapacitors. Angew Chem Int Ed. 2015;54(6):1868-72.
- [24] Xiao J, Yang S. Sequential crystallization of sea urchin-like bimetallic (Ni, Co) carbonate hydroxide and its morphology conserved conversion to porous NiCo₂O₄ spinel for pseudocapacitors. RSC Adv. 2011:1(4):588-95.
- [25] Wang L, Jiao X, Liu P, Ouyang Y, Xia X, Lei W, et al. Self-template synthesis of yolk-shelled NiCo₂O₄ spheres for enhanced hybrid supercapacitors. Appl Surf Sci. 2018;427:174-81.
- [26] Chouke PB, Potbhare AK, Meshram NP, Rai MM, Dadure KM, Chaudhary K, et al. Bioinspired NiO nanospheres: exploring in vitro toxicity using bm-17 and L. rohita liver cells, DNA degradation, docking, and proposed vacuolization mechanism. ACS Omega. 2022:7(8):6869-84.
- [27] Seol M, Lee M, Kim H, Shin KW, Cho Y, Jeon I, et al. High-throughput growth of wafer-scale monolayer transition metal dichalcogenide via vertical Ostwald ripening. Adv Mater. 2020;32(42):2003542.
- Park GD, Kim JH, Kang YC. Lithium-ion storage performances of sunflower-like and nano-sized hollow SnO₂ spheres by spray pyrolysis and the nanoscale Kirkendall effect. Nanoscale. 2018;10(28):13531-8.
- Yang Y, Güder F, Zacharias M. Diffusion-induced void evolution in core-shell nanowires: elaborated view on the nanoscale Kirkendall effect. Isr J Chem. 2010;50(4):439-48.
- Zhao J, Zou Y, Zou X, Bai T, Liu Y, Gao R, et al. Self-template construction of hollow Co₃O₄ microspheres from porous ultrathin nanosheets and efficient noble metal-free water oxidation catalysts. Nanoscale. 2014;6(13):7255-62.
- Anderson BD, Tracy IB. Nanoparticle conversion chemistry: Kirkendall effect, galvanic exchange, and anion exchange. Nanoscale. 2014;6(21):12195-216.

- [32] Chaudhary RG, Juneja HD, Gharpure MP. Thermal degradation behaviour of some metal chelate polymer compounds with bis (bidentate) ligand by TG/DTG/DTA. J Therm Anal Calorim. 2013;112(2):637–47.
- [33] Li Y, Cheng G, Zhou Z, Liao X, Han S, Ye F, et al. Shape-controlled synthesis of NiCo₂O₄-rGO as bifunctional electrocatalyst for zn-air battery. ChemElectroChem. 2019;6(17):4429–36.
- [34] Lim D, Kong H, Lim C, Kim N, Shim SE, Baeck S-H. Spinel-type $NiCo_2O_4$ with abundant oxygen vacancies as a high-performance catalyst for the oxygen reduction reaction. Int J Hydrog Energy. 2019;44(42):23775–83.
- [35] Guo J, Yin Z, Zang X, Dai Z, Zhang Y, Huang W, et al. Facile one-pot synthesis of $NiCo_2O_4$ hollow spheres with controllable number of shells for high-performance supercapacitors. Nano Res. 2017:10:405–14.
- [36] Yuan H, Li J, Yang W, Zhuang Z, Zhao Y, He L, et al. Oxygen vacancy determined highly efficient oxygen reduction in NiCo₂O₄/hollow carbon spheres. ACS Appl Mater Interfaces. 2018;10(19):16410–7.
- [37] Zhu C, Fu S, Du D, Lin Y. Facilely tuning porous NiCo₂O₄ nanosheets with metal valence-state alteration and abundant oxygen vacancies as robust electrocatalysts towards water splitting. Chem – Eur J. 2016;22(12):4000–7.
- [38] Natile MM, Glisenti A. Study of surface reactivity of cobalt oxides: interaction with methanol. Chem Mater. 2002;14:3090–9.
- [39] Kim J-G, Pugmire DL, Battaglia D, Langell MA. Analysis of the NiCo₂O₄ spinel surface with auger and x-ray photoelectron spectroscopy. Appl Surf Sci. 2002;14(7):3090–9.
- [40] Qian L, Gu L, Yang L, Yuan H, Xiao D. Direct growth of ${\rm NiCo_2O_4}$ nanostructures on conductive substrates with enhanced electrocatalytic activity and stability for methanol oxidation. Nanoscale. 2013;5(16):7388–96.
- [41] Marco JF, Gancedo JR, Gracia M, Gautier JL, Ríos E, Berry FJ. Characterization of the nickel cobaltite, NiCo₂O₄, prepared by several methods: An XRD, XANES, EXAFS, and XPS study. J Solid State Chem. 2000;153(1):74–81.
- [42] Bao J, Zhang X, Fan B, Zhang J, Zhou M, Yang W, et al. Ultrathin spinel-structured nanosheets rich in oxygen deficiencies for

- enhanced electrocatalytic water oxidation. Angew Chem Int Ed. 2015;127(25):7507–12.
- [43] Hu J, Zhao X, Chen W, Chen Z. Enhanced charge transport and increased active sites on α-Fe₂O₃ (110) nanorod surface containing oxygen vacancies for improved solar water oxidation performance. ACS Omega. 2018;3(11):14973–80.
- [44] Ge H, Li G, Zheng T, Wang F, Shao M, Liu H, et al. Hollow NiCo₂O₄ nanospheres supported on N-doped carbon nanowebs as efficient bifunctional catalyst for rechargeable and flexible zn-air batteries. Electrochim Acta. 2019;319:1–9.
- [45] Dong M, Liu X, Jiang L, Zhu Z, Shu Y, Chen S, et al. Cobalt-doped Mn₃O₄ nanocrystals embedded in graphene nanosheets as a highperformance bifunctional oxygen electrocatalyst for rechargeable zn-air batteries. Green Energy Environ. 2020;5(4):499–505.
- [46] Askari MB, Rozati SM, Salarizadeh P, Saeidfirozeh H, Di, Bartolomeo A. A remarkable three-component RuO₂-MnCo₂O₄/ rGO nanocatalyst towards methanol electrooxidation. Int J Hydrogen Energy. 2021;46(74):36792–800.
- [47] Wang W, Yang Y, Luo H, Hu T, Wang F, Liu W. Ultrasound-assisted preparation of titania–alumina support with high surface area and large pore diameter by modified precipitation method. J Alloy Compd. 2011;509(7):3430–4.
- [48] Zhang Y, Ma J, Ma M, Zhang C, Jia X, Wang G. Co and Co₉S₈ nanoparticles uniformly embedded in S, N-doped porous carbon as electrocatalysts for rechargeable zinc-air batteries. J Mater Res Technol. 2022;18:3764–76.
- [49] Hou D, Zhang J, Tian H, Li Q, Li C, Mai Y. Pore engineering of 2D mesoporous nitrogen-doped carbon on graphene through block copolymer self-assembly. Adv Mater Interfaces. 2019;6(24):1901476.
- [50] Wei W, Liang H, Parvez K, Zhuang X, Feng X, Müllen K. Nitrogendoped carbon nanosheets with size-defined mesopores as highly efficient metal-free catalyst for the oxygen reduction reaction. Angew Chem Int Ed. 2014;126(6):1596–600.
- [51] Pahalagedara MN, Pahalagedara LR, Kuo C-H, Dharmarathna S, Suib SL. Ordered mesoporous mixed metal oxides: remarkable effect of pore size on catalytic activity. Langmuir. 2014;30(27):8228–37.